Coupled Aeropropulsive Design Optimization of a Boundary Layer Ingestion Propulsor

Justin S. Gray and Joaquim R. R. A. Martins

Abstract

Airframe-propulsion integration concepts that use boundary layer ingestion have the potential to reduce aircraft fuel burn. One concept that has been recently explored is NASA's STARC-ABL aircraft configuration, which offers the potential for fuel burn reduction by using a turboelectric propulsion system with an aft-mounted electrically driven boundary layer ingestion (BLI) propulsor. So far, attempts to quantify this potential fuel burn reduction have not considered the full coupling between the aerodynamic and propulsive performance. To address the need for a more careful quantification of the aeropropulsive benefit of the STARC-ABL concept, we run a series of design optimizations based on a fully coupled aeropropulsive model. A 1-D thermodynamic cycle analysis is coupled to a Reynolds-averaged Navier-Stokes simulation to model the aft propulsor at a cruise condition and the effects variation in propulsor design on overall performance. A series of design optimization studies are performed to minimize the required cruise power, assuming different relative sizes of the BLI propulsor. The design variables consist of the fan pressure ratio, static pressure at the fan face, and 311 variables that control the shape of both the nacelle and the fuselage. The power required by the BLI propulsor is compared with a podded configuration. The results show that the BLI configuration offers 6% to 9% reduction in required power at cruise, depending on assumptions made about the efficiency of power transmission system between the under-wing engines and the aft propulsor. Additionally, the results indicate that the power transmission efficiency directly effects the relative size of the under-wing engines and the aft propulsor. This design optimization, based on computational fluid dynamics, is shown to be essential to evaluate current BLI concepts and provides a powerful tool for the design of future concepts.

Nomenclature

A_{ref}	wing reference area
BLI	boundary layer ingestion
C_D	drag from the lifting surfaces of the aircraft
C_{F_x}	net force coefficient in the axial direction on the fuselage and aft propulsor
$C_{F_{\text{pod}}}$	net force coefficient in the axial direction on an isolated propulsor
FFD	free form deformation
IDF	individual design feasible optimization architecture
$\dot{m}$	mass flow rate
p_s	static pressure
p_t	total pressure
$\text{Pwr}_{\text{shaft}}$	shaft power delivered to a propulsor
T_t	total temperature
V_∞	freestream velocity
$()^{\text{FE}}$	flow quantities at the fan exit
$()^{\text{FF}}$	flow quantities at the fan face
$()^*$	target design values used by the IDF optimization formulation
$()'$	quantities computed on the podded reference configuration

Greek Symbols

ρ_∞	freestream density
η_a	fan adiabatic efficiency
η_{trans}	power transmission efficiency
$\mathcal{G}$	geometric shape constraints
$\mathcal{R}$	residual equations

1   Introduction

In 1947, Smith and Roberts[1] proposed embedding the inlets of turbine engines into an aircraft fuselage so that they would draw off low momentum boundary layer air and forestall the turbulent transition. They proposed that the aeropropulsive interactions of boundary layer ingestion (BLI) could provide a synergistic benefit to aircraft performance. At the time, their concept was not developed further for aviation applications, but subsequent research focused on maritime applications was performed by Wislicenus[2], Betz[3], and Gearhart and Henderson[4]. Their collective work established wake-ingesting propulsors as an efficient propulsion system design for torpedo and other marine applications. In 1993, interest in BLI applications to aircraft design was renewed when Smith[5] introduced the concept of the power saving coefficient (PSC) to measure the improvement relative to a non-BLI baseline, which he defined as

$$\text{PSC} = \frac{\text{Pwr}'_{\text{shaft}} - \text{Pwr}_{\text{shaft}}}{\text{Pwr}'_{\text{shaft}}}. \tag{1}$$

This metric compared the power required by the BLI configuration ($\text{Pwr}_{\text{shaft}}$) to the power of a reference podded configuration ($\text{Pwr}'_{\text{shaft}}$). Comparing performance based on

the power is useful because, as Betz[3] showed, the more traditional metric of propulsive efficiency is ill defined for BLI applications, since it can have values greater than 1. Smith further noted that using power as the metric to compare BLI and traditional propulsion systems was important because traditional metrics based on thrust and drag accounting are difficult to apply in a coupled aeropropulsive application. Higher values of PSC indicate greater relative efficiency for a BLI versus a traditional propulsion system. Smith estimated PSC values as high as 0.5 for certain configurations, indicating that a BLI could offer a 50% reduction in energy usage relative to a traditional podded configuration. Drela[6], recognizing the inherent challenge of using traditional thrust-drag bookkeeping for BLI applications, proposed a power balance accounting system that uses a well defined set of terms regardless of propulsion system configuration.

The potential for a large reduction in energy usage has motivated conceptual design studies of various aircraft configurations with BLI propulsion systems, predicting fuel burn reductions from 4% to 10%[7,8,9,10,11]. All of these studies attempt to capture the effects of BLI by estimating the boundary layer profile on the fuselage without the propulsor present and then superimposing a propulsor inlet over it to estimate the effective inlet properties for the propulsion system. BLI creates a fully coupled aeropropulsive system, but the superposition approach only captures the aerodynamic effects on the propulsion system. The effect of the propulsion system on the aerodynamics is not captured. To achieve this analytical decoupling, we must make assumptions about either the aerodynamics or propulsion models. For example, Hardin et al.[12] analyzed the effect of BLI on a traditional turbofan using a 1-D thermodynamic analysis by assuming the engine was embedded into the boundary layer computed by solving the Reynolds-averaged Navier–Stokes equations (RANS) for a clean fuselage, thus assuming that the boundary layer is unchanged by the presence of the engine.

Recent wind tunnel tests on the D8 configuration have demonstrated strong coupling effects, including changes to the aircraft pitching moment as a function of throttle setting and asymmetries in shaft power between adjacent propulsors[13]. Prior work by the authors has demonstrated that fully coupled aeropropulsive models predict significantly different propulsor inlet conditions compared to models that assume the aerodynamics are unaffected by the presence of the propulsor[14]. That work, along with the recent wind tunnel experiments, have proven that a coupled analysis approach is necessary when analyzing the performance of a given BLI design. Since fully coupled aeropropulsive models are necessary in order to accurately analyze BLI systems, it follows that it is equally necessary to consider such models in the design of such systems. Furthermore, we hypothesize that there are trades to be made between the under-wing and aft propulsors, and between the aerodynamic and propulsion disciplines, which can only be done optimally when using the coupled aeropropulsive model and varying all design variables involved simultaneously. The goal of this work is to show that this is the case.

To achieve the goal stated above, we create a fully coupled aeropropulsive model of the BLI propulsor mounted on the aft of an axisymmetric fuselage to perform a propulsion sizing study on NASA's STARC-ABL concept, shown in Figure 1[11]. The STARC-ABL has three propulsors: two traditional under-wing turbofans and an aft-mounted BLI propulsor. The BLI propulsor is an electrically driven fan powered by
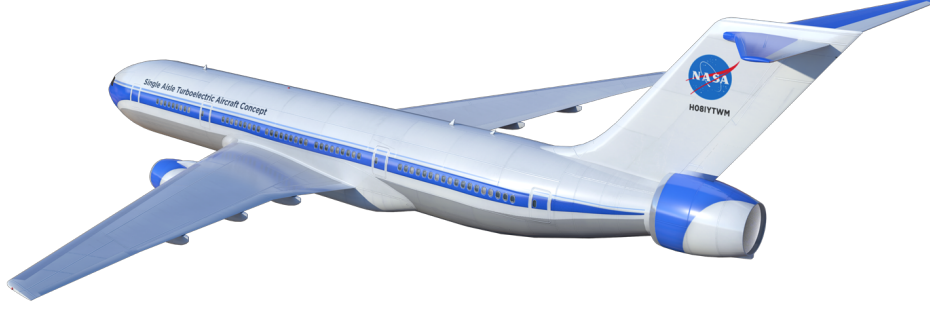
Figure 1: The STARC-ABL aircraft configuration uses a propulsor mounted in the aft of the fuselage that ingests the boundary layer.

generators attached to the low-speed spools from the two under-wing turbofans. This paper presents a sizing analysis for the STARC-ABL aircraft that focuses on the relative sizes of the under-wing and BLI propulsors. This sizing is accomplished using a two-phased modeling approach. In the first phase, the aeropropulsive fuselage is analyzed in isolation from the rest of the aircraft to study the performance of the BLI propulsor. We create a reference podded configuration with a bare fuselage and a podded propulsor ingesting freestream air to serve as a reference configuration for comparison. Using the OpenMDAO framework[15,16,17], we perform a series of design optimizations that minimize the shaft power subject to a constraint on the net force coefficient for the fuselage. The optimizations are performed for a range of different values of net force constraint for both the BLI and podded configurations. In the second phase, the data from the optimized BLI and podded propulsors is combined to estimate the best overall power split between the under-wing and aft-mounted propulsors, assuming that the aircraft is at a steady cruise condition. The results show that the BLI configuration offers 6% to 9% reduction in required power at cruise, depending on the assumptions made about the efficiency of the system that transfers the power between the under-wing engines and the aft propulsor.

2 Design Optimization of the Aeropropulsive Fuselage

2.1 Aerodynamic Model

The aerodynamic analysis consists of solving the RANS equations using ADflow[18] in a 2-D axisymmetric domain. ADflow is a second order, finite-volume CFD solver that provides adjoint analytic derivatives[19]. Together with a gradient-based optimization algorithm, this enables efficient design optimization with respect to a large number of design variables[20]. This CFD solver has been extensively validated for transonic flight conditions against wind tunnel data provided by the 2017 AIAA Drag Prediction Workshop[21], and mesh convergence studies have verified the second order convergence of the solver for a range of different meshes[22]. To simplify the analysis, the STARC-ABL aircraft is separated into fuselage (including the aft propulsor) and lifting surface components. A representative fuselage is sized to be similar to that of a Boeing 737-900

in length and diameter. We consider two fuselage configurations: a BLI configuration and a podded configuration. The podded configuration provides a reference against which we can compare the BLI propulsor performance.

The BLI configuration consists of a single integrated geometry with the propulsor attached to the aft part of the fuselage. Figure 2 shows this configuration with labels for the four boundary conditions: viscous walls (S_1, S_2), outflow face (S_3), and inflow face (S_4). The surfaces S_3 and S_4 represent the interface between the propulsion and aerodynamic models, and appropriate boundary conditions must be applied on these surfaces. The outflow boundary condition on S_3 is a prescribed uniform static pressure. This assumption is consistent with boundary layer theory, which assumes a constant static pressure at the surface. The total pressure variation caused by the boundary layer and the associated velocity variation is thus carried out of the flow domain as a non-uniform flow at S_3. The inflow boundary condition on S_4 is defined by a prescribed uniform p_t and T_t, which ultimately is defined by the propulsion model, so while the outflow condition allows for flow non-uniformity, the inflow condition does not. This means that the model assumes that the flow exiting the fan is well mixed. The mesh for this axisymmetric analysis has 170,000 cells, and each CFD solution takes approximately two minutes when using a quad-core workstation with 2.8 GHz processors.
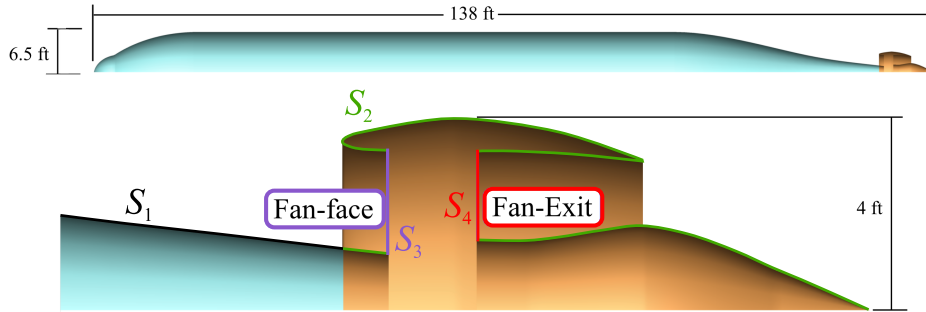

Figure 2: BLI configuration and boundary conditions: viscous walls (S_1, S_2), outflow face (S_3), and inflow face (S_4)

The podded configuration consists of two separate surfaces: one for the fuselage, and another for the podded propulsor. Figure 3 shows each of these surfaces. The main body of the fuselage is identical in both configurations. Similarly, the nacelle shape and plug shape are also identical for the two configurations. The bare propulsor model performance predictions are used to estimate the under-wing propulsor performance as well.

For both configurations, the geometry is parameterized via free-form deformation (FFD) to modify the surface mesh[23]. The surface changes are propagated to the volume grid using an inverse distance weighted method of mesh deformation[24]. The majority of the fuselage shape remains fixed, but the shape of the aft taper section and of the nacelle and plug are allowed to vary. The FFD boxes and associated control points are shown in Figure 4 for the BLI configuration. The podded configuration uses
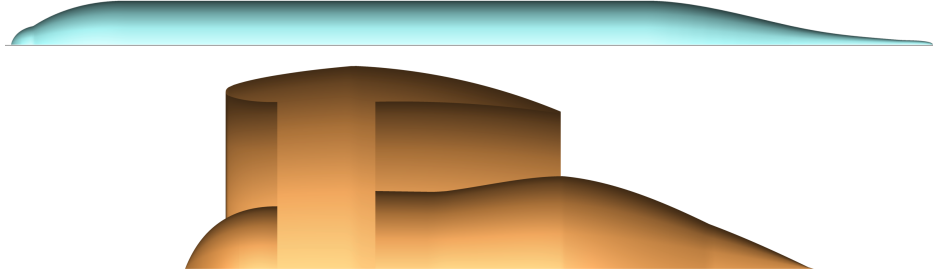
Figure 3: The podded configuration serves as a reference and models fuselage (top) and propulsor (bottom) separately.

the same FFD on the propulsor section (shown in orange) but keeps the clean fuselage unchanged.
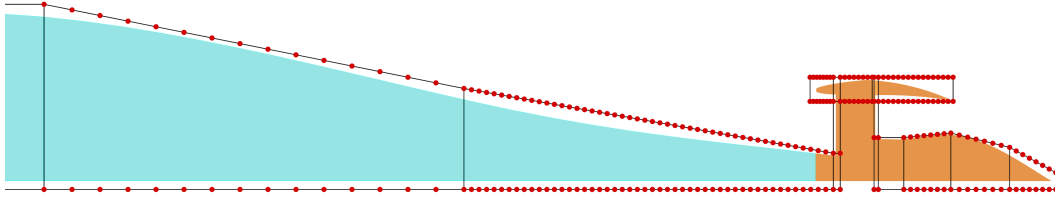

Figure 4: The shape of the BLI configuration is enveloped in FFD boxes (black lines) and parameterized using FFD control points.

One of the major challenges when modeling BLI propulsion systems is establishing a consistent scheme for bookkeeping all of the forces on the combined aeropropulsive system when some of the forces are computed by the aerodynamic analysis and other forces are computed by the propulsion analysis. We avoid this problem by computing all the forces within only the aerodynamic analysis using the following equation:

$$
C_{F_x} = \frac{2}{\rho_\infty V_\infty^2 A_{\text{ref}}} \left(\iint_{S_1} (p\hat{\boldsymbol{n}} + \boldsymbol{f}_{\text{visc}}) \cdot \hat{\boldsymbol{x}} dS + \iint_{S_2} (p\hat{\boldsymbol{n}} + \boldsymbol{f}_{\text{visc}}) \cdot \hat{\boldsymbol{x}} dS + \iint_{S_3} \left(p\hat{\boldsymbol{n}} \cdot \hat{\boldsymbol{x}} + \rho_3 u_3^2 \right) dS + \iint_{S_4} \left(p\hat{\boldsymbol{n}} \cdot \hat{\boldsymbol{x}} - \rho_4 u_4^2 \right) dS \right), \quad (2)
$$

which accounts for all of the viscous, pressure, and momentum flux forces on the entire body. Each contribution is color coded to match the associated boundary condition in Fig. 2. Note that the sign of C_{F_x} is significant: A positive value indicates a net decelerating force (i.e., drag) on the body, and a negative value indicates a net accelerating force (i.e., thrust). The reference values used for Eq. (2) are given in Table 1.

2.2 Propulsion Model

The propulsion analysis is performed using a 1-D thermodynamic model implemented in pyCycle[25,26], a modular thermodynamic cycle modeling tool built in OpenMDAO[15]. This tool provides a flexible cycle modeling capability similar to the industry

Table 1: Reference values used in the force nondimensionalization

ρ_∞	0.0008 slug/ft^3
V_∞	707.3 ft/sec
A_{ref}	1,400 ft^2

standard NPSS[27] tool; however, unlike NPSS, pyCycle provides analytic derivatives, which were necessary for the gradient-based optimizations that we perform in this work.
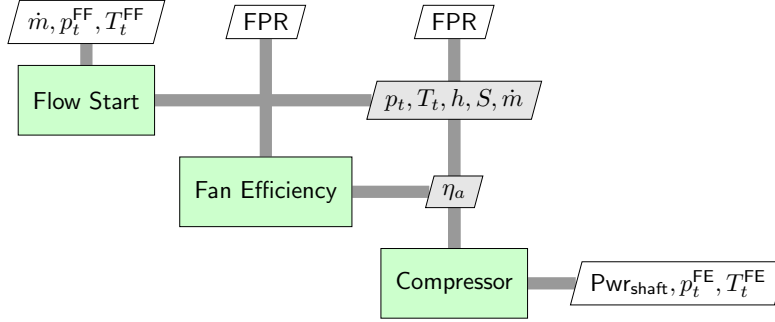

Figure 5: The propulsor fan model consists of three sub-models; It computes the shaft power and fan exit conditions given the FPR, mass flow, and fan face conditions.

The propulsor fan is modeled with three separate parts, as shown in the XDSM diagram[28] (Fig. 5). The flow-start computes the enthalpy (h) and entropy (s) given mass flow rate ($\dot{m}$), mass-averaged total temperature (T_t^{FF}), and mass-averaged total pressure (p_t^{FF}) from the fan face (S_3 in Fig. 2). The fan pressure ratio (FPR) is also given as an input and will be one of the design variables in the optimization. The model outputs fan exit total temperature (T_t^{FE}), total pressure (p_t^{FF}), and the required shaft power to handle the given mass flow rate. The fan efficiency is computed using a linear correlation with FPR,

$$\eta_a = 1.066 - 0.0866 \cdot \mathrm{FPR}, \tag{3}$$

where the constants were chosen to yield a 96.2% efficiency for FPR= 1.2 and 95% efficiency for FPR= 1.4. This linear fit for fan adiabatic efficiency is derived from data published in two studies on next-generation subsonic transport aircraft for the NASA Advanced Air Transport Technologies Project[29,30]. Eq. (3) captures the change in fan performance as the design fan pressure ratio changes, but it does not account for the impact of inlet distortion caused by the boundary layer ingestion. The 2-D aerodynamic analysis used here does not accurately capture inlet distortion, so the impact of distortion is not modeled in this work. Ongoing work with 3-D aerodynamic models will account for this impact[31].

2.3 Optimization Problem

To capture the aeropropulsive interactions, we build a fully coupled model of the fuselage and BLI propulsor by combining the aerodynamic and propulsion models in the OpenMDAO framework. OpenMDAO was selected for several reasons. As mentioned above, the pyCycle tool itself is built in OpenMDAO, which makes the framework the natural choice for the larger multidisciplinary integration. In addition, OpenMDAO supports an MPI-based, distributed memory data storage that is necessary to efficiently integrate the ADflow aerodynamics analysis. Lastly, both ADflow and pyCycle provide analytic derivatives, and OpenMDAO is able to automatically compute the multidisciplinary adjoint derivatives for the coupled model, which saves development time for our application. The availability of adjoint analytic derivatives enables us to use efficient gradient-based optimization to handle the high-dimensional design space of the combined aeropropulsive design problem. In this work, we use a sequential quadratic programming (SQP) optimizer implemented in the SNOPT[32] package, which is integrated into the OpenMDAO framework via the pyOptSparse Python wrapper[33].

The aeropropulsive coupling is implemented using an individual design feasible (IDF) optimization architecture[34], which uses constraints imposed on the final solution to enforce multidisciplinary compatibility. There are four IDF constraints represented by $\mathcal{R}_{\mathrm{Pwr}}$, $\mathcal{R}_{p_t^{FE}}$, $\mathcal{R}_{T_t^{FE}}$, and $\mathcal{R}_{\dot{m}}$ in Fig. 6 that force the target values—any value with the $()^*$ superscript—to match the values computed using the actual models. We use the same optimization problem formulation for both the BLI and the podded configurations. The grids for the aerodynamic analysis are different between the two configurations, as shown in Fig. 2 (BLI configuration) and Fig. 3 (podded configuration).
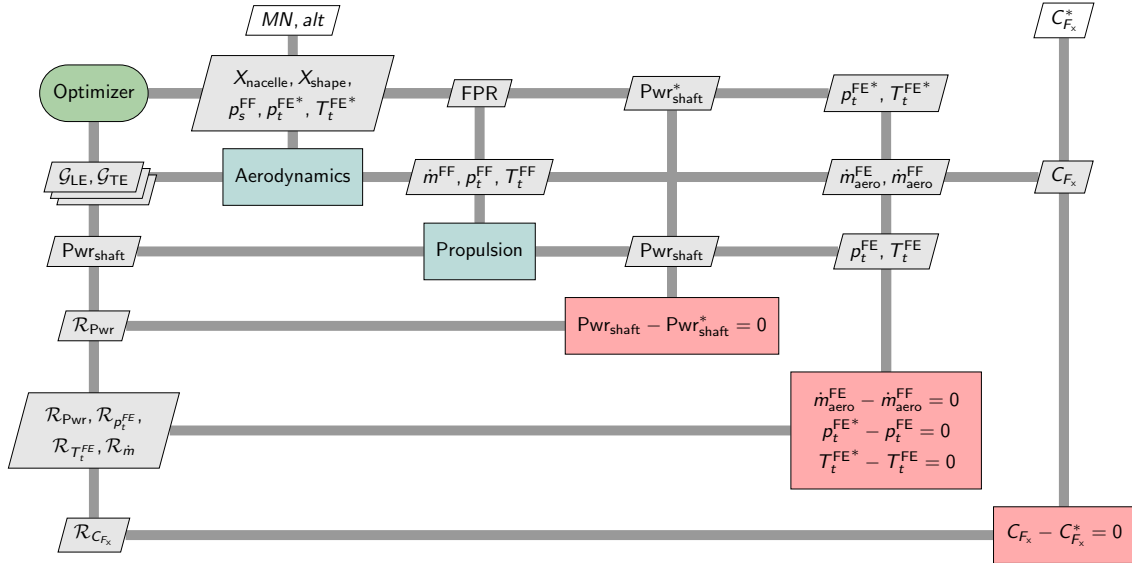

Figure 6: XDSM diagram of the full optimization problem formulation, including the compatibility constraints that enforce the aeropropulsive coupling.

The goal of the optimization is to minimize $\mathrm{Pwr}_{\mathrm{shaft}}$ with respect to FPR, static

pressure at the fan face $\left(p_s^{\text{FF}}\right)$, and 311 aerodynamic shape variables $(X_{\text{nacelle}}, X_{\text{shape}})$, subject to a prescribed net force $\left(C_{F_x}^*\right)$ on the fuselage. The FPR is allowed to vary from 1.2 to 1.5. These bounds are applied to keep the fan designs within a reasonable range. The shape variables have no upper bound but are given lower bounds based on the limits of the mesh deformation algorithm. Specifically, the lower limits prevent the nozzle plug from being forced to shrink below a minimum radius.

The optimization problem formulation is detailed in Table 2. In addition to the design variables mentioned above, there are three additional design variables listed in Table 2: $\text{Pwr}_{\text{shaft}}^*$, $p_t^{\text{FE}*}$, and $T_t^{\text{FE}*}$); however, these are not true design degrees of freedom because they are used by the optimizer to satisfy the IDF constraints. Two sets of geometric constraints ($\mathcal{G}_{\text{LE}}$ and $\mathcal{G}_{\text{TE}}$) are imposed on the leading and trailing edge of the propulsor nacelle profile to ensure that the optimizer does not make them unrealistically thin.

In Fig. 6, the C_{F_x} constraint appears similar to the four IDF constraints, except that the target value $\left(C_{F_x}^*\right)$ is given as a parameter external to the optimization. This constraint is not needed for multidisciplinary compatibility, but instead it is used to ensure a well posed optimization problem. This constraint is needed because we do not know a priori what the relative size of the BLI and under-wing propulsors should be. Depending on what the optimal sizing turns out to be, the net force on the fuselage could range from a net drag to a net thrust. Because we do not know the thrust split, a constraint on net force is required in order to ensure a unique solution to the design optimization problem.

In the first phase of this work, we perform a sweep of optimizations for a range of $C_{F_x}^*$ values. In the second phase, using the data from these optimizations, we find the most efficient size for the BLI propulsor.

2.4 Aeropropulsive Optimization Results

Two sets of 13 optimizations are performed for different net thrust constraint values, ranging from $C_{F_x}^* = 0.0025$ to $C_{F_x}^* = -0.156$, corresponding to 3000 N net drag and 17 000 N net thrust, respectively. One set of optimizations is run on the BLI configuration, and a second set is run on the podded configuration to serve as a reference. All of the optimized configurations had an FPR of 1.2, which was the lower bound for that design variable. The PSC, defined in Eq. (1), is computed for each net thrust coefficient value by using the shaft power for the optimized podded configuration as the reference ($\text{Pwr}'_{\text{shaft}}$). Figure 7 shows that the PSC takes a maximum value of 0.202 for $C_{F_x} = 0.0025$ and that the PSC decreases smoothly to 0.093 for $C_{F_x} = -0.156$. At $C_{F_x} = 0.0025$, there is a slight net decelerating force on the fuselage, which corresponds to a small BLI propulsor. Conversely, $C_{F_x} = -0.156$ yields a net accelerating force on the fuselage, which corresponds to a larger BLI propulsor. Note that the results in Fig. 7 are computed only on the fuselage and BLI propulsor. In the next section, we extend this problem to estimate the sizing for the whole propulsion system, including the under-wing propulsors.

Table 2: Optimization problem for the fuselage aeropropulsive design.

	Variable/Function	Description	Quantity
minimize	$\mathrm{Pwr}_{\mathrm{shaft}}$	Propulsor shaft power	
with respect to	FPR	Fan pressure ratio	1
	X_{nacelle}	Global nacelle shape variables	3
	X_{shape}	Nacelle and fuselage local shape variables	308
	p_s^{FF}	Static pressure at the fan face	1
	$\mathrm{Pwr}_{\mathrm{shaft}}^*$	Propulsor shaft power target	1
	p_t^{FE*}	Total pressure target at the fan exit	1
	T_t^{FE*}	Total temperature target at the fan exit	1
		Total	316
subject to	$C_{F_x}^{\mathrm{net}} = C_{F_x}^{\mathrm{net}*}$	Specified net force on full body	1
	$\mathcal{R}_{\dot{m}} = 0$	mass flow IDF constraint	1
	$\mathcal{R}_{\mathrm{Pwr}} = 0$	Propulsor shaft power IDF constraint	1
	$\mathcal{R}_{p_t^{FE}} = 0$	Total pressure IDF constraint	1
	$\mathcal{R}_{T_t^{FE}} = 0$	Total temperature IDF constraint	1
	$0.9 < \mathcal{G}_{\mathrm{LE}} < 2$	Leading edge thickness	3
	$0.9 < \mathcal{G}_{\mathrm{TE}} < 2$	Trailing edge thickness	3
		Total	11
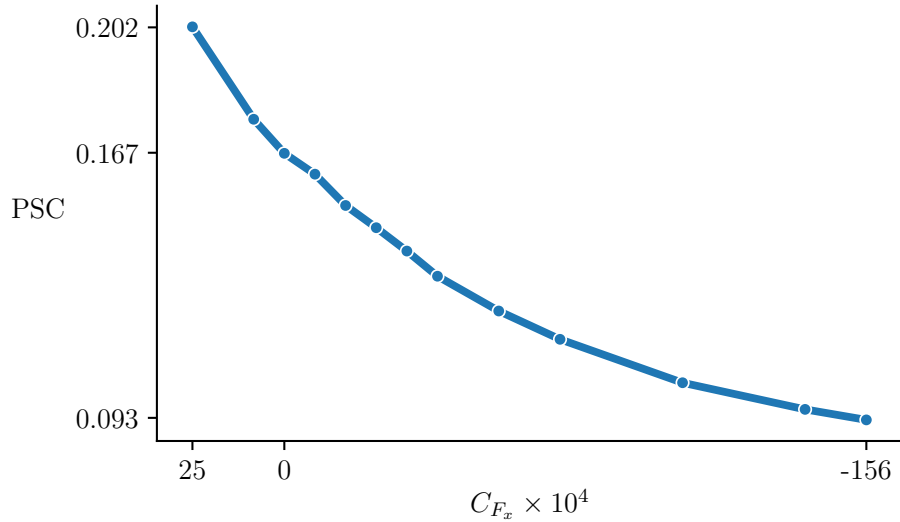
Figure 7: Power saving coefficient versus C_{F_x} shows that smaller BLI propulsors (small positive C_{F_x}) offer greater power savings than larger ones.

3 BLI Propulsor Sizing Analysis

3.1 Podded Propulsor Performance

Although traditional thrust and drag accounting is not valid for the BLI configuration, the podded configuration can still be examined using a force-based metric because in that case, the propulsor and fuselage are two separate items; thus, the propulsor thrust ($C_{F_{\mathrm{pod}}}$) is a well defined quantity, computed using Eq. (2) applied to the podded propulsor surfaces (the orange surfaces in Fig. 3). Figure 8 plots the data for each of the optimized podded propulsors normalized by counts of net force on the propulsor. Given that FPR= 1.2 for all of the optimized configurations, from a pure thermodynamic cycle analysis perspective, one would expect a flat line in Fig. 8; however, since the thrust data computed here includes the nacelle drag it represents installed thrust and some dependence on nacelle diameter is expected.
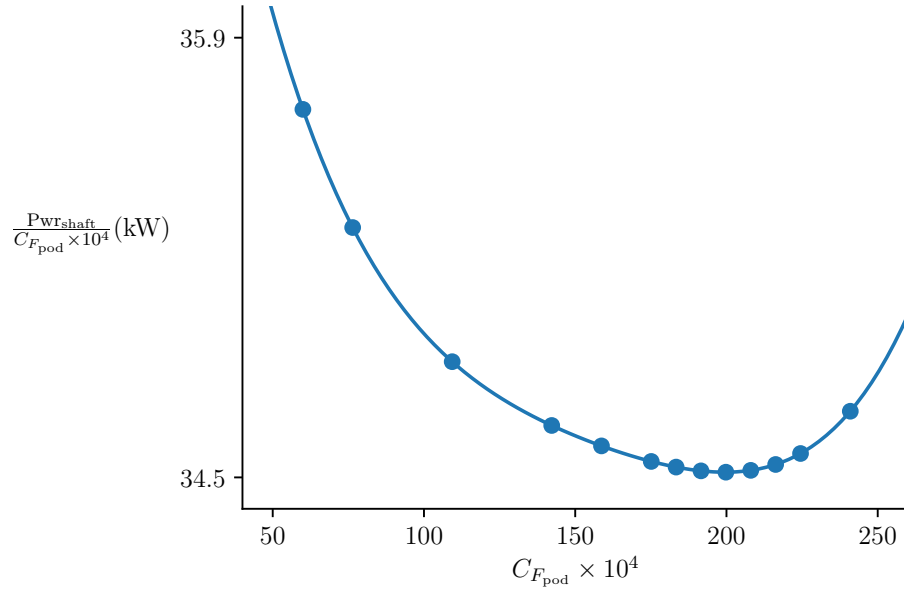

Figure 8: $\mathrm{Pwr}_{\mathrm{shaft}}/C_{F_{\mathrm{pod}}}$ data (circles) and 4$^{\text{th}}$ order polynomial fit (solid line) for the podded propulsor.

The solid line in Fig. 8 is a 4$^{\text{th}}$ order polynomial fit of the data, given by

$$\frac{\mathrm{Pwr}_{\mathrm{shaft}}}{C_{F_{\mathrm{pod}}} \times 10^4} = 38.89 - 0.00867x + 7.474 \times 10^{-4}x^2 - 3.013 \times 10^{-6}x^3 + 4.729 \times 10^{-9}x^4. \quad (4)$$

This equation can be used to predict the required shaft power. For any podded engine thrust value, we should stay within the bounds of the fitted data to avoid extrapolation issues. One caveat with this equation is that it was fit based on results from a single under-wing propulsor, so when applying it to compute power requirements for the whole aircraft, it is important to consider that there are two engines and hence each one only produces half the thrust and hence half the force coefficient.

3.2 Propulsion System Sizing Method

Equation (2) computes only the force coefficient on the fuselage component of the aircraft. To size the propulsion system, we must consider additional drag contributions from the lifting surfaces—wings, vertical tail, and horizontal tail. This lifting surface drag is computed using the empirical drag methods in the FLOPS tool[35], using appropriate inputs for the STARC-ABL configuration. In this case, FLOPS predicts a lifting surface drag of 216 counts ($C_D = 0.0216$).

At a steady cruise condition, the aircraft should remain at a constant speed, meaning that the net force is zero. With the assumed C_D and any prescribed value of C_{F_x}, we can compute the required additional force coefficient from the under-wing propulsors that satisfy this zero-net-force constraint as follows

$$C_{F_{\mathrm{pod}}} = -(C_D + C_{F_x}), \tag{5}$$

where, as previously mentioned, the sign of the force coefficients is significant: Positive values result in deceleration and negative impart acceleration.

By combining Eqs. (4) and (5), we compute the required shaft power from the under-wing propulsors. To provide a reference, we use the net drag on the clean fuselage from the podded configuration and assume that 100% of the thrust—and hence all of the required shaft power—is generated by the under-wing engines. For each optimized BLI fuselage design, the C_{F_x} is known because it is prescribed as an optimization constraint; therefore, the required additional shaft power from the under-wing propulsors can be computed using Eq. (5) for each BLI configuration. To compute the total required shaft power for the BLI configuration at cruise, we can use the following relationship,

$$\mathrm{Pwr}_{\mathrm{tot}} = \frac{\mathrm{Pwr}_{\mathrm{BLI}}}{\eta_{\mathrm{trans}}} + \mathrm{Pwr}_{\mathrm{pod}}, \tag{6}$$

where we take into account the combined transmission efficiency, η_{trans}. This is the efficiency of the system that generates the power from the under-wing engines and transmits it to the aft fuselage to power the electric drive motor. Three values for η_{trans} are considered: 0.9, 0.95, and 0.98. An η_{trans} of 0.9 represents the expected transmission efficiency for a traditional AC/DC power system[11]. The values for η_{trans} of 0.95 and 0.98 are assumed for future performance of systems based on the use of superconducting motors, generators, and power lines. The percentage reduction in power consumption at cruise for a fuselage with a particular C_{F_x} and assumed η_{trans} can then be computed by taking the ratio of the power required for the BLI configuration to the reference power required for the configuration without BLI (the podded configuration).

3.3 Propulsion Sizing Results

Figure 9 shows the combined results from the analysis described by Eqs. (4), (5), and (6) plotted versus the power split between the aft BLI propulsor and the under-wing propulsors. The results show that the optimal propulsor sizing depends strongly on the assumed value for η_{trans}. Assuming current power transmission technology levels (i.e., $\eta_{\mathrm{trans}} = 0.9$), BLI yields a 1% reduction in net shaft power required at cruise, and

the aft propulsor uses 15.3% of the total power. This small improvement in overall performance is significantly lower than the 9% to 20% improvement in the standalone BLI propulsor seen in Fig. 7. This makes it clear that η_{trans} is having a massive effect on overall system performance. Losing 10% of the power by converting mechanical energy to electrical and back to mechanical is driving the overall system to a very small BLI propulsor, which is limiting the overall effect on overall fuel burn.

As η_{trans} improves, the overall results improve as well. For $\eta_{\text{trans}} = 0.95$, PSC values of 2% to 2.5% are achieved across the whole range of power splits. These results are notable for the large flat plateau to the right of the optimum power split of 34.3%, which implies that there is a large amount of design freedom in terms of aft propulsor sizing. In the best case scenario, $\eta_{\text{trans}} = 0.98$, the best PSC occurs at the largest power split analyzed. At very high η_{trans}, this result is expected because the best performance would come from making as much thrust from the BLI propulsor as possible.
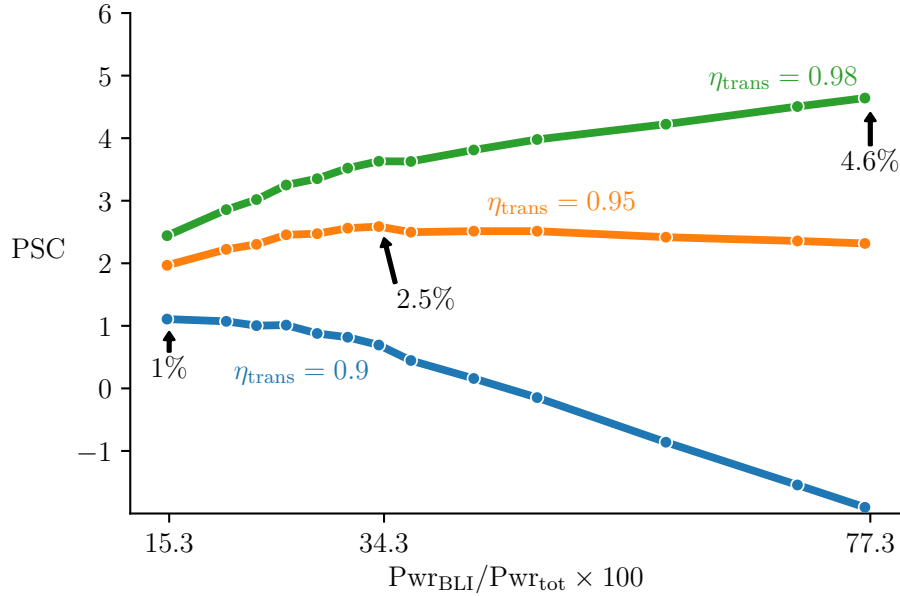

Figure 9: Overall aircraft PSC at cruise vs the fraction of shaft power used for BLI at different assumed values of transmission efficiency, η_{trans}.

We must emphasize that this sizing analysis is done from a purely thermodynamic perspective. The optimum power split between the BLI and under-wing propulsors is estimated considering only the aeropropulsive effects and the overall power usage of the system. Furthermore, only a single cruise condition is examined. A complete aircraft design process would need to consider other factors, including the overall mass of the turboelectric propulsion system with respect to BLI propulsor size, multiple flight conditions, thermal performance for the power transmission system, tail rotation angle at takeoff, and center of gravity movement. Additionally, the axisymmetric analysis done here does not account for impact of the wing and tail on the inflow conditions of the BLI propulsor. Despite missing these elements in the analysis, these results do provide a conclusive picture of how the propulsion system performance is affected by

the inclusion of a BLI propulsor, and how the optimum sizing of that propulsion system varies with changes in electric power transmission efficiency.

3.4 Qualitative Analysis of the Optimized Configurations

Figure 10 compares the optimal power split designs for $\eta_{\text{trans}} = (0.9, 0.95, 0.98)$. The most notable change between the three designs is the size of the aft propulsor, which grows significantly as the assumed transmission efficiency improves. The outermost streamline of the flow entering the propulsor is shown as a black line on each design. For $\eta_{\text{trans}} = 0.98$, the propulsor is very large and is clearly ingesting non-boundary layer flow. Closer examination of the nacelle and nozzle plug shapes between the three cases shows significant differences in shape between each case. The nozzle plug shows the greatest variation in shape, with a nearly flat profile for the smallest propulsor and the development of the ramp shape to create a stronger nozzle throat as the propulsor grows. The nacelle also changes shape, though more subtly. As the nacelle moves up into the faster moving flow, it takes on a slightly larger tilt to better align with the local flow and becomes slightly thicker. These shape variations highlight the importance of using an optimization-based design approach for this coupled problem. The aerodynamic analysis is sensitive to these small changes in the shape, and hence the overall trends that are reported are sensitive to them as well, and an optimizer is required to make sure each design considered in the parametric sweep is performing as well as it can.

The variation in the Mach contours between each design in Fig. 10 is worth discussing. There are two places where these variations are most significant and obvious. The flow over the top of the nacelle changes dramatically as the propulsor grows larger. For $\eta_{\text{trans}} = 0.9$, the nacelle is effectively in the shadow of the fuselage and the nacelle wall sees very low speed flow. As the nacelle grows bigger, the flow becomes faster, and the high speed region over the top of it grows larger. This variation in flow results in a variation in the amount of viscous drag on the nacelle for the BLI case that is greater than was observed for the podded configuration in clean flow.

The second flow feature that displays variation with changing propulsor is the boundary layer profile near the inlet of the propulsor. We examined the variation in the flow over the aft fuselage due to the presence of the propulsor in greater detail in prior work[?]; however, that work performed only aeropropulsive analysis for a fixed nacelle shape. Those results indicated that, although the flow field was changed with a variation in the inlet height, the trends were sensitive to p_s^{FF}, which we acknowledged could change in a final optimized result if nacelle shape was allowed to change. Figure 11 examines the boundary layer profiles—defined using the total pressure ratio with freestream—half a meter ahead of the inlet lip for the best design found for each assumed value of η_{trans}. Total pressure ratio is used to define the boundary layer, rather than the more traditional velocity metric, because the flow around the tailcone is undergoing inviscid diffusion, which makes a comparison with the freestream velocity inaccurate. The edge of the boundary layer is denoted by the vertical red dashed line at $p_t/p_{t\infty} = 0.99$. In Fig. 11, the largest propulsor design (corresponding to $\eta_{\text{trans}} = 0.98$) shows a pronounced difference in boundary layer profile compared to the two smaller
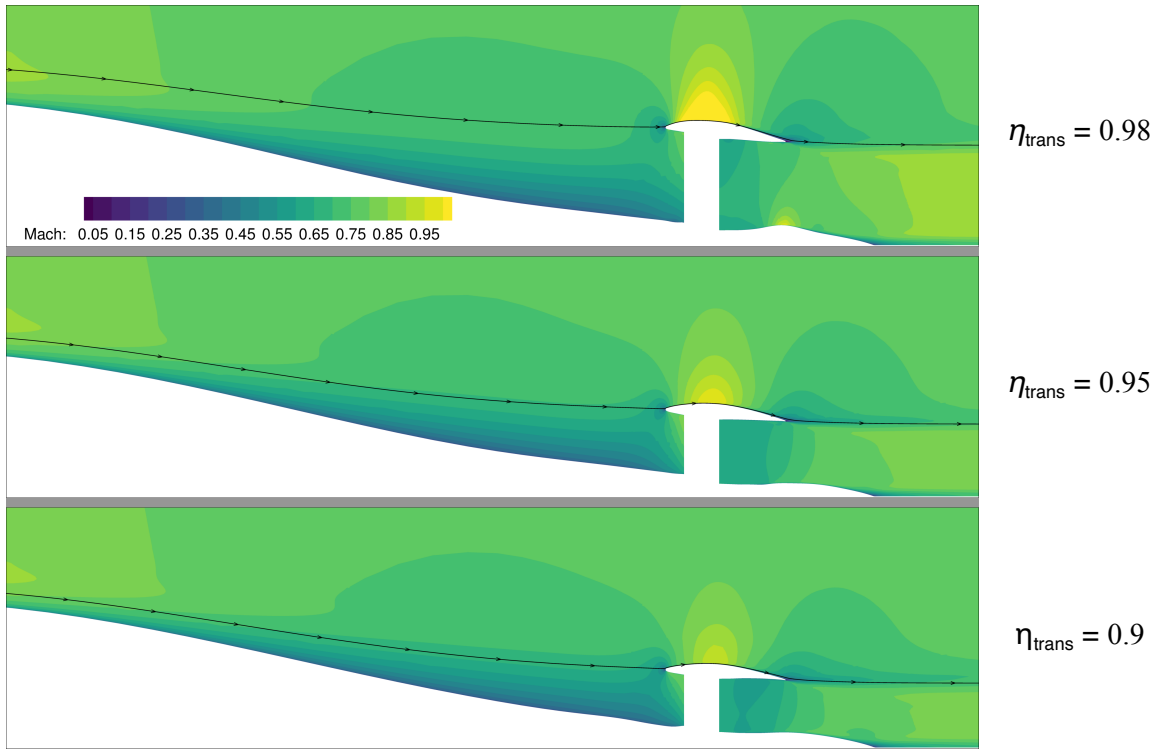
Figure 10: Best-performing designs for three assumed values of η_{trans}. Increased transmission efficiency drives the design to larger BLI propulsors relative to the under-wing engines.
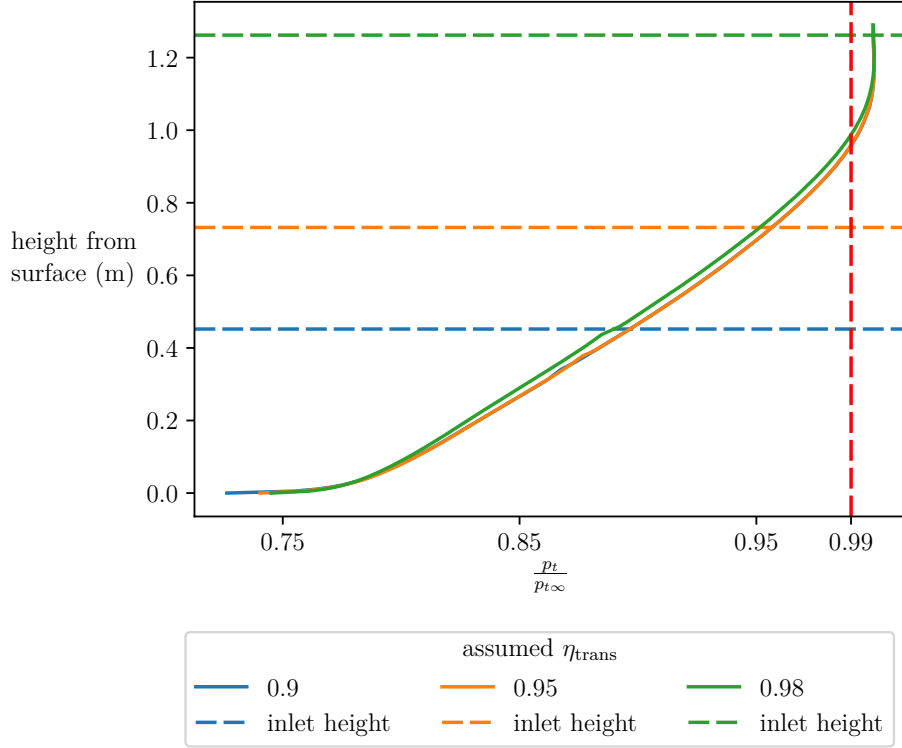
Figure 11: Boundary layer profiles (measured via $p_t/p_{t\infty}$) for the best designs found for each assumed value of η_{trans}. The horizontal dashed lines indicate the height of the inlet lip for each design.

designs. The larger propulsor applies a greater backpressure to the flow, which causes the boundary layer to grow thicker. We can also clearly see from the horizontal dashed lines that denote the inlet height for each design that the largest propulsor ingests a significant amount of flow from outside the boundary layer. The two smaller propulsors, however, ingest only boundary layer flow. Although the profiles for the two smaller propulsors look very similar, there is a small difference very close to the fuselage where variations in the surface pressure distribution become apparent. Overall, these results show less variation in the boundary layer profile than prior work, but it is clear that the aeropropulsive coupling still has an impact on the boundary layer near the propulsor.

4   Conclusions

A series of design optimizations of a simplified version of NASA's STARC-ABL aircraft configuration were performed using a fully coupled aeropropulsive model. The goal of the STARC-ABL configuration is to utilize an aft-mounted, electrically-driven BLI propulsor to achieve a significant reduction in mission fuel burn. The aircraft configuration was simplified by representing the fuselage and aft-mounted propulsor as an axisymmetric body. The aerodynamic model of the fuselage and propulsor combination was based on a RANS CFD model, and this was coupled with a 1-D thermodynamic

16

model of the propulsor fan via outflow and inflow boundary conditions that modeled the fan face and fan exit, respectively. The coupling was formulated using an IDF formulation so that it was enforced as part of the optimization. The entire model was constructed and optimized using gradient-based optimization with analytic derivatives in the OpenMDAO framework. The shaft power was minimized, with respect to both aerodynamic shape variables and propulsion design variables while enforcing a prescribed constraint on the net force of the fuselage and propulsor combination. A series of optimizations was performed with different values for the net force constraint for both a BLI and a reference podded configuration for the aft-mounted propulsor.

The performance of the BLI propulsor was measured by comparing the required power of the optimized BLI configuration to that of the optimized podded configuration for the same net force on the overall body (i.e., computing the PSC). This comparison showed that smaller propulsors achieved the best PSC. For small values of net drag on the fuselage, the BLI configuration had a PSC of 0.202. A PSC value of .202, or a 20.2% reduction in required shaft power, seemingly represents a significant potential savings, however this point also corresponds to the smallest BLI propulsor design. The BLI propulsors were found to get progressively less efficient as they grew in size, reaching a minimum power savings coefficient of 0.093 for the largest propulsor.

The variation in PSC as a function of propulsor sizing is significant because it means that the designs with the highest PSC values do not necessarily translate to the best overall design of the propulsion system because the STARC-ABL only gets part of its thrust from the aft-mounted BLI propulsor. Despite being significantly more efficient, the smaller BLI propulsors produce a smaller portion of the overall thrust, and hence can only reduce the energy usage of the whole propulsion system by a small amount. In order to identify the best overall design for the whole propulsion system, we performed a propulsion sizing analysis by examining the combined power requirements of both the BLI propulsor, accounting for the effect of power transmission efficiency, and under-wing engines to provide a metric of overall efficiency. The sizing analysis indicated that, assuming current electrical power transmission technology, 1% power savings is achieved when 15.3% of the aircraft power is transmitted to the aft propulsor. Using a moderately advanced power transmission system with an efficiency of 95%, the optimum PSC reaches .025. As an extremely high power transmission efficiency of 98%, the best performance is achieved by making as much thrust as possible from the BLI propulsor.

The aeropropulsive analysis and design performed for this work demonstrates the importance of using fully coupled models to predict the performance of physically coupled systems. The standalone BLI propulsor analysis shows a large potential efficiency gain from this aeropropulsive concept. The challenge is to integrate BLI technology into an aircraft configuration to make the most of it. Analysis of the full propulsion system for the STARC-ABL configuration shows that propulsion-airframe integration will have a large impact on the overall performance. There are two key coupling effects that each affect how the full propulsion system performs. First, the aeropropulsive effects on the BLI propulsor are shown to vary in strength as a function of propulsor sizing which, contributes to a nonlinear variation in BLI benefit. Second, the impact of electrical power transmission efficiency is shown to have a first order effect on the

relative sizing of the under-wing vs BLI propulsors. Although they can be described separately, in reality these two coupling effects cannot be considered in isolation of each other in the context of aeropropulsive design. As one varies the power transmission efficiency, the propulsion system must be redesigned to maximize benefits and the relative sizing of the under-wing and BLI propulsors can vary significantly.

5   Acknowledgments

References

[1] Smith, A. M. O. and Roberts, H. E., "The Jet Airplane Utilizing Boundary Layer Ingestion for Propulsion," *Journal of Aeronautical Sciences*, Vol. 14, No. 2, 1947, pp. 97–109.

[2] Wislicenus, G. F., "Hydrodynamics and Propulsion of Submerged Bodies," *Journal of the American Rocket Society*, Vol. 30, December 1960, pp. 1140–1148.

[3] Betz, A., *Introduction to the Theory of Flow Machines*, Pergamon Press, 1966.

[4] Gearhart, W. S. and Henderson, R. E., "Selection of a Propulsor for a Submersible System," *Journal of Aircraft*, Vol. 3, No. 1, 1966, pp. 84–90.

[5] Smith, L. H., "Wake Ingestion Propulsion Benefit," *Journal of Propulsion and Power*, Vol. 9, No. 1, February 1993, pp. 74–82, 10.2514/6.1991-2007.

[6] Drela, M., "Power Balance in Aerodynamic Flows," *AIAA Journal*, Vol. 47, No. 7, 2009, pp. 1761–1771, 10.2514/1.42409.

[7] Felder, J. L., Kim, H. D., and Brown, G. V., "Turboelectric Distributed Propulsion Engine Cycle Analysis for Hybrid-Wing-Body Aircraft," *47th AIAA Aerospace Sciences Meeting including The New Horizons Forum and Aerospace Exposition*, AIAA 2009-1132, 2009, 10.2514/6.2009-1132.

[8] Drela, M., "Development of the D8 Transport Configuration," *9th AIAA Applied Aerodynamics Conference*, AIAA 2011-3970, 2011, 10.2514/6.2011-3970.

[9] Liu, C., Doulgeris, G., Laskaridis, P., and Singh, R., "Thermal cycle analysis of turboelectric distributed propulsion system with boundary layer ingestion," *Aerospace Science and Technology*, Vol. 27, No. 1, 2013, pp. 163 – 170, http://dx.doi.org/10.1016/j.ast.2012.08.003.

[10] Laskaridis, P., Pachidis, V., and Pilidis, P., "Opportunities and challenges for distributed propulsion and boundary layer ingestion," *Aircraft Engineering and Aerospace Technology*, Vol. 86, No. 6, 2014, pp. 451–458, 10.1108/AEAT-05-2014-0067.

[11] Welstead, J. R. and Felder, J. L., "Conceptual Design of a Single-Aisle Turboelectric Commercial Transport with Fuselage Boundary Layer Ingestion," *54th AIAA Aerospace Sciences Meeting*, AIAA 2016-1027, 2016, 10.2514/6.2016-1027.

[12] Hardin, L., Tillman, G., Sharma, O., Berton, J., and Arend, D., "Aircraft System Study of Boundary Layer Ingesting Propulsion," *48th AIAA/ASME/SAE/ASEE Joint Propulsion Conference and Exhibit*, AIAA-2012-2993, 2012, 10.2514/6.2012-3993.

[13] Uranga, A., Drela, M., Greitzer, E. M., Hall, D. K., Titchener, N. A., Lieu, M. K., Siu, N. M., Casses, C., Huang, A. C., Gatlin, G. M., , and Hannon, J. A., "Boundary Layer Ingestion Benefit of the D8 Transport Aircraft," *AIAA Journal*, Vol. in press.

[14] S.Gray, J., Mader, C. A., Kenway, G. K. W., and Martins, J. R. R. A., "Modeling Boundary Layer Ingestion Using a Coupled Aeropropulsive Analysis," *Journal of Aircraft*, Vol. 55, 2018, pp. 1191–1199, 10.2514/1.C034601.

[15] Gray, J. S., Hearn, T. A., Moore, K. T., Hwang, J. T., Martins, J. R. R. A., and Ning, A., "Automatic Evaluation of Multidisciplinary Derivatives Using a Graph-Based Problem Formulation in OpenMDAO," *15th AIAA/ISSMO Multidisciplinary Analysis and Optimization Conference*, American Institute of Aeronautics and Astronautics, August 2014, 10.2514/6.2014-2042.

[16] Hwang, J. T., *A Modular Approach to Large-Scale Design Optimization of Aerospace Systems*, Ph.D. thesis, University of Michigan, 2015.

[17] Hwang, J. T. and Martins, J. R. R. A., "A computational architecture for coupling heterogeneous numerical models and computing coupled derivatives," *ACM Transactions on Mathematical Software*, Vol. 44, No. 4, June 2018, pp. Article 37, 10.1145/3182393.

[18] Lyu, Z., Kenway, G. K. W., and Martins, J. R. R. A., "Aerodynamic Shape Optimization Investigations of the Common Research Model Wing Benchmark," *AIAA Journal*, Vol. 53, No. 4, April 2015, pp. 968–985, 10.2514/1.J053318.

[19] Lyu, Z., Kenway, G. K., Paige, C., and Martins, J. R. R. A., "Automatic Differentiation Adjoint of the Reynolds-Averaged Navier–Stokes Equations with a

Turbulence Model," *21st AIAA Computational Fluid Dynamics Conference*, San Diego, CA, Jul. 2013, 10.2514/6.2013-2581.

[20] Martins, J. R. R. A. and Hwang, J. T., "Review and Unification of Methods for Computing Derivatives of Multidisciplinary Computational Models," *AIAA Journal*, Vol. 51, No. 11, November 2013, pp. 2582–2599, 10.2514/1.J052184.

[21] Coder, J. G., Pulliam, T. H., Hue, D., Kenway, G. K., and Sclafani, A. J., "Contributions to the 6th AIAA CFD Drag Prediction Workshop Using Structured Grid Methods," *AIAA SciTech Forum*, American Institute of Aeronautics and Astronautics, Jan. 2017. doi:10.2514/6.2017-0960.

[22] Kenway, G. K. W., Secco, N. R., Martins, J. R. R. A., Mishra, A., and Duraisamy, K., "An Efficient Parallel Overset Method for Aerodynamic Shape Optimization," *Proceedings of the 58th AIAA/ASCE/AHS/ASC Structures, Structural Dynamics, and Materials Conference, AIAA SciTech Formum*, January 2017, 10.2514/6.2017-0357.

[23] Kenway, G. K., Kennedy, G. J., and Martins, J. R. R. A., "A CAD-Free Approach to High-Fidelity Aerostructural Optimization," *Proceedings of the 13th AIAA/ISSMO Multidisciplinary Analysis Optimization Conference*, No. AIAA 2010-9231, Fort Worth, TX, Sept. 2010, 10.2514/6.2010-9231.

[24] Luke, E., Collins, E., and Blades, E., "A fast mesh deformation method using explicit interpolation," *Journal of Computational Physics*, Vol. 231, No. 2, 2012, pp. 586 – 601, 10.1016/j.jcp.2011.09.021.

[25] Gray, J., Chin, J., Hearn, T., Hendricks, E., Lavelle, T., and Martins, J. R. R. A., "Chemical Equilibrium Analysis with Adjoint Derivatives for Propulsion Cycle Analysis," *Journal of Propulsion and Power*, Vol. 33, No. 5, September 2017, pp. 1041–1052, 10.2514/1.B36215.

[26] Hearn, D. T., Hendricks, E., Chin, J., Gray, J., and Moore, D. K. T., "Optimization of Turbine Engine Cycle Analysis with Analytic Derivatives," *17th AIAA/ISSMO Multidisciplinary Analysis and Optimization Conference, part of AIAA Aviation 2016 (Washington, DC)*, 2016, 10.2514/6.2016-4297.

[27] Jones, S., *An Introduction to Thermodynamic Performance Analysis of Aircraft Gas Turbine Engine Cycles Using the Numerical Propulsion System Simulation Code*, 2007, NASA TM-2007-214690.

[28] Lambe, A. B. and Martins, J. R. R. A., "Extensions to the Design Structure Matrix for the Description of Multidisciplinary Design, Analysis, and Optimization Processes," *Structural and Multidisciplinary Optimization*, Vol. 46, 2012, pp. 273–284, 10.1007/s00158-012-0763-y.

[29] Greitzer, E., Bonnefoy, P., la Rosa Blanco, E. D., Dorbian, C., Drela, M., Hall, D., Hansman, R., Hileman, J., Liebeck, R., Lovegren, J., Mody, P., Pertuze, J.,

Sato, S., Spakovszky, Z., Tan, C., Hollman, J., Duda, J., Fitzgerald, N., Houghton, J., Kerrebrock, J., Kiwada, G., Kordonowy, D., Parrish, J., Tylko, J., Wen, E., and Lord, W., "N+3 Aircraft Concept Designs and Trade Studies, Final Report," NASA CR 2010-216794, National Aeronautics and Space Administration, 2010.

[30] Bradley, M. K. and Droney, C. K., "Subsonic Ultra Green Aircraft Research: Phase I Final Report," NASA CR 2011-216847, National Aeronautics and Space Administration, 2011.

[31] Gray, J. S., Kenway, G. K. W., and Martins, J. R. R. A., "Aero-propulsive Design Optimization of a Turboelectric Boundary Layer Ingestion Propulsion System," *2018 AIAA/ISSMO Multidisciplinary Analysis and Optimization Conference*, Atlanta, GA, AIAA 2018-3976, June 2018.

[32] Gill, P. E., Murray, W., and Saunders, M. A., "SNOPT: An SQP Algorithm for Large-Scale Constrained Optimization," *SIAM Rev.*, Vol. 47, No. 1, Jan. 2005, pp. 99–131, 10.1137/S0036144504446096.

[33] Perez, R. E., Jansen, P. W., and Martins, J. R. R. A., "pyOpt: a Python-Based Object-Oriented Framework for Nonlinear Constrained Optimization," *Structural and Multidisciplinary Optimization*, Vol. 45, 2012, pp. 101–118, 10.1007/s00158-011-0666-3.

[34] Martins, J. R. R. A. and Lambe, A. B., "Multidisciplinary Design Optimization: A Survey of Architectures," *AIAA Journal*, Vol. 51, 2013, pp. 2049–2075, 10.2514/1.J051895.

[35] McCullers, L. A., "Aircraft configuration optimization including optimized flight profiles," NASA CR CP-2327, National Aeronautics and Space Administration, 1984.